Superfluid-superradiant mixed phase of the interacting degenerate Fermi gas in an optical cavity

Feng YanLin, Zhang Kuang, Fan JingTao, Mei Feng, Chen Gang and Jia SuoTang

Citation: SCIENCE CHINA Physics, Mechanics & Astronomy **61**, 123011 (2018); doi: 10.1007/s11433-018-9271-5

View online: http://engine.scichina.com/doi/10.1007/s11433-018-9271-5

View Table of Contents:http://engine.scichina.com/publisher/scp/journal/SCPMA/61/12

Published by the Science China Press

SCIENCE CHINA
Physics, Mechanics & Astronomy

SCIENCE CHINA
Physics, Mechanics & Astronomy

• Article •

December 2018 Vol. 61 No. 12: 123011
https://doi.org/10.1007/s11433-018-9271-5

Superfluid-superradiant mixed phase of the interacting degenerate Fermi gas in an optical cavity

YanLin Feng[1,2], Kuang Zhang[1,2], JingTao Fan[1,2], Feng Mei[1,2], Gang Chen[1,2*], and SuoTang Jia[1,2]

[1] *State Key Laboratory of Quantum Optics and Quantum Optics Devices, Institute of Laser Spectroscopy, Shanxi University, Taiyuan 030006, China;*
[2] *Collaborative Innovation Center of Extreme Optics, Shanxi University, Taiyuan 030006, China*

Received May 18, 2018; accepted June 27, 2018; published online August 30, 2018

We investigate the ground-state properties of an attractively interacting degenerate Fermi gas coupling with a high-finesse optical cavity. We predict a new mixed phase with both the superfluid and superradiant properties for the intermediate fermion-fermion interaction and fermion-photon coupling strengths. Moreover, in this mixed phase a relatively large ratio of the scaled polarization to the dimensionless mean-field gap, which is in contrast to that in the conventional superfluid regime can be obtained. We also figure out rich phase diagrams depending crucially on the atomic resonant frequency (effective Zeeman field) and address briefly the experimental detection of our predicted quantum phases.

degenerate Fermi gas, superfluid, superradiant, optical cavity

PACS number(s): 03.75.Ss, 05.30.Fk, 32.80.-t, 32.90.+a, 42.50.Pq

Citation: Y. L. Feng, K. Zhang, J. T. Fan, F. Mei, G. Chen, and S. T. Jia, Superfluid-superradiant mixed phase of the interacting degenerate Fermi gas in an optical cavity, Sci. China-Phys. Mech. Astron. **61**, 123011 (2018), https://doi.org/10.1007/s11433-018-9271-5

1 Introduction

The experimental coupling of a Bose-Einstein condensate with a high-finesse optical cavity opens a new way to explore novel many-body physics and process quantum information [1]. A notable example is that a second-order phase transition from a normal phase to a superradiant (SR) phase, which was predicted more than 40 years ago [2, 3], can be observed successfully [4-6]. In the normal phase, the atoms or photons are unexcited while macroscopically excited in the SR phase. It is therefore essential for the quantum simulation of condensed matter and many-body physics [7, 8]. In contrast to bosons which can occupy the same quantum state, only one fermion can occupy a particular quantum state, due to the Pauli exclusion principle. As a result, it is natural to ask a fundamental question what new physics can arise when degenerate Fermi gas interacts with a high-finesse optical cavity. Motivated by near-term experimental prospects, the interplay between the noninteracting degenerate Fermi gas and the optical cavity has been considered theoretically [9-20]. It has been found that at moderate and high densities the Fermi statistics plays a leading role in the SR phase transition [10-12]. In addition, cavity-induced topological states [13-16], a cavity-induced artificial magnetic field [17], and a normal-SR phase [18] have been predicted.

In fact, for degenerate Fermi gas there exists an intriguing interaction between fermions, which can be tuned by a magnetic-field dependent Feshbach resonance [21-23]. When the interaction is attractive, two fermions with the opposite momenta and different spins can form the Cooper pair and the system exhibits an exotic superfluid (SF) [24-26]. Recently, the coupling of attractively interacting degenerate Fermi gas coupling with the high-finesse optical cavity has been taken into account [27, 28], and a filling-density-

*Corresponding author (email: chengang971@163.com)

depended SR phase transition, which is mostly enhanced in the SF regime, has been predicted [27].

In this paper, we consider a similar setup and mainly reveal the competition between the conventional superfluidity and the superradiance by studying the ground-state properties under the mean-field approximation. For the intermediate fermion-fermion interaction and fermion-photon coupling strengths, we predict a new mixed phase with both the SR and SF properties and a first-order quantum phase transition from the SR to the SF phases. Moreover, in this mixed phase we achieve a relatively large ratio of the scaled polarization to the dimensionless mean-field gap, which is also in contrast to that in the conventional SF regime. We also figure out rich phase diagrams depending crucially on the atomic resonant frequency (effective Zeeman field). Finally, we address briefly how to detect the predicted quantum phases and phase diagrams in experiments.

2 Model and Hamiltonian

We consider the attractively interacting degenerate Fermi gas coupling with a high-finesse optical cavity. As shown in Figure 1(a), an ensemble of one-dimensional ultracold four-level fermions (blue) are coupled to a far-of-resonance optical trap (yellow) of the yz plane by a tightly-radial confinement along the x direction. The cavity field is driven by a linearly-polarized driving laser (red line) with frequency $\omega_{\rm l}$. The fermions are pumped by two left- and right-circular polarized transverse pumping lasers (green line) with frequency $\omega_{\rm p}$. The driving laser and two pumping lasers induce two Raman processes. The magnetic field $\mathbf{B}$ is going along the positive z axis known as the quantization axis and generates a Zeeman shift between two hyperfine ground states. Figure 1(b) shows the atomic energy levels and their transitions. Each atom has two ground states $|\uparrow\rangle$ and $|\downarrow\rangle$ and two excited states $|1\rangle$ and $|2\rangle$. The $|\downarrow\rangle \longleftrightarrow |1\rangle$ and $|\uparrow\rangle \longleftrightarrow |2\rangle$ transitions (red solid lines) are caused by the quantized cavity field with fermion-photon coupling strength g. Whereas, the transverse pumping lasers govern the $|\uparrow\rangle \longleftrightarrow |1\rangle$ and $|\downarrow\rangle \longleftrightarrow |2\rangle$ transitions (green dashed lines) with Rabi frequency Ω. The pump frequency $\omega_{\rm p}$ is close to that of the cavity frequency $\omega_{\rm c}$, but both of them are far-red detuned with respect to the frequencies of two excited states $\omega_{1,2}$.

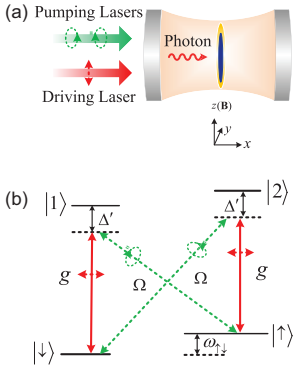

Figure 1 (Color online) (a) Proposed schematic setup; (b) the atomic energy levels and their transitions.

In the regime $\Delta' = \omega_{1,2} - \omega_{\rm p} \gg \{g, \Omega\}$, the two excited states $|1\rangle$ and $|2\rangle$ can be adiabatically eliminated from the dynamics of our system. Then the system is described by the total 2D Hamiltonian for the atomic ground states which is written as:

$$\begin{aligned}\hat{H} =&\omega\hat{a}^{\dagger}\hat{a} + \sum_{\mathbf{k}} \xi_{\mathbf{k}} \hat{C}^{\dagger}_{\mathbf{k},\sigma}\hat{C}_{\mathbf{k},\sigma} + \frac{\eta}{\sqrt{n}}\sum_{\mathbf{k}}\left(\hat{C}^{\dagger}_{\mathbf{k},\uparrow}\hat{C}_{\mathbf{k},\downarrow}\right.\\ &\left.+\hat{C}^{\dagger}_{\mathbf{k},\downarrow}\hat{C}_{\mathbf{k},\uparrow}\right)\left(\hat{a}+\hat{a}^{\dagger}\right) + \omega_0\sum_{\mathbf{k}}\left(\hat{C}^{\dagger}_{\mathbf{k},\uparrow}\hat{C}_{\mathbf{k},\uparrow} - \hat{C}^{\dagger}_{\mathbf{k},\downarrow}\hat{C}_{\mathbf{k},\downarrow}\right)\\ &+\lambda\sum_{\mathbf{k}}\hat{C}^{\dagger}_{\mathbf{k},\uparrow}\hat{C}^{\dagger}_{-\mathbf{k},\downarrow}\hat{C}_{-\mathbf{k},\downarrow}\hat{C}_{\mathbf{k},\uparrow}, \end{aligned} \tag{1}$$

where $\hat{a}^{\dagger}$ and $\hat{a}$ are the creation and annihilation operators of the quantized cavity field, $\omega = n\zeta + \omega_{\rm c} - \omega_{\rm l}$ is the atom-number dependent cavity frequency with $\zeta = |g|^2/\Delta$ and $\omega_{\rm c}$ the frequency of the cavity field, $\hat{C}^{\dagger}_{\mathbf{k},\sigma}$ and $\hat{C}_{\mathbf{k},\sigma}$ are the creation and annihilate operators of the fermionic fields with the momentum $\mathbf{k}$ and the internal states $\sigma = \uparrow, \downarrow$, $\xi_{\mathbf{k}} = \epsilon_{\mathbf{k}} - \mu$ with the kinetic energy $\epsilon_{\mathbf{k}} = \mathbf{k}^2/2M$, $\omega_0 = (\omega_{\uparrow} - \omega_{\downarrow})/2$ is the effective Zeeman field, η is the effective fermion-photon coupling strength, $n = K_{\rm F}^2/(2\pi) = E_{\rm F}M/\pi$ is the density of fermions in 2D with the Fermi momentum $K_{\rm F}$ and the Fermi energy $E_{\rm F} = K_{\rm F}^2/(2M)$, and λ is the negative interaction strength (i.e., $\lambda < 0$). When $\lambda = 0$, the Hamiltonian (1) is the same as eq. (12) in our previous discussion [20]. When $\eta = 0$, the Hamiltonian (1) describes the polarized Fermi superfluidity which has been widely discussed in the refs. [29-32].

It is important that all parameters in the Hamiltonian (1) can be flexibly controlled. For example, both ω_0 and ω can be tuned by modifying the frequencies of the driving laser and the transverse pumping lasers, while η can be controlled via the Rabi frequencies of the transverse pumping lasers. Besides, λ can be tuned by varying the s-wave scattering length $a_{\rm s}$ through the Feshbach resonant technique [22].

3 Ground-state properties

In order to investigate the ground-state properties of the Hamiltonian (1), we first introduce the mean-field SF order parameter called the gap, $\Delta = \lambda\sum_{\mathbf{k}}\left\langle\hat{C}_{-\mathbf{k},\downarrow}\hat{C}_{\mathbf{k},\uparrow}\right\rangle$ [33, 34], to rewrite the two-body interacting Hamiltonian as $\hat{H}_{\rm INT} = \Delta\sum_{\mathbf{k}}\left(\hat{C}_{-\mathbf{k},\downarrow}\hat{C}_{\mathbf{k},\uparrow} + \hat{C}^{\dagger}_{\mathbf{k},\uparrow}\hat{C}^{\dagger}_{-\mathbf{k},\downarrow}\right) - \Delta^2/\lambda$. For simplicity, the mean-field gap is here assumed to be real, i.e., $\Delta = \Delta^*$. In ad-

dition, our considered system usually exists the cavity decay rate κ, and thus, we should consider the Hesienberg-Langevin equation for the cavity field operator $\hat{a}$, i.e., $\mathrm{i}\partial\hat{a}/\partial t = (\omega - \mathrm{i}\kappa)\hat{a} + \left(\eta/\sqrt{n}\right)\sum_k \hat{C}^\dagger_{\mathbf{k},\uparrow}\hat{C}_{\mathbf{k},\downarrow} + \hat{C}^\dagger_{\mathbf{k},\downarrow}\hat{C}_{\mathbf{k},\uparrow}$. Since the inverse of the cavity field decay rate κ is much small than the time scales of system dynamics, the cavity field can reach a steady state on a much faster time scale than the external atomic motion, i.e., $\partial\hat{a}/\partial t = 0$. Then under the mean-field approach, the steady-state solution of $\alpha = \langle\hat{a}\rangle$ is given by $\alpha = \langle\hat{a}\rangle = \eta\sum_k\left\langle\hat{C}^\dagger_{\mathbf{k},\uparrow}\hat{C}_{\mathbf{k},\downarrow} + \hat{C}^\dagger_{\mathbf{k},\downarrow}\hat{C}_{\mathbf{k},\uparrow}\right\rangle / \left[\sqrt{n}\left(-\omega + \mathrm{i}\kappa\right)\right]$. Notice that $|\alpha|^2$ is nonezero in the SR phase and is thus called the SR order parameter.

Based on above discussions and the approximation $\hat{a} \approx \langle\hat{a}\rangle$, the Hamiltonian (1) turns into

$$\hat{H} = \frac{1}{2}\sum_{\mathbf{k}}\hat{\Psi}^\dagger_{\mathbf{k}}M_{\mathbf{k}}\hat{\Psi}_{\mathbf{k}} + \sum_{\mathbf{k}}\xi_{\mathbf{k}} - \frac{\Delta^2}{\lambda} + \omega|\alpha|^2, \tag{2}$$

where $\hat{\Psi}_{\mathbf{k}} = \left(\hat{C}_{\mathbf{k},\uparrow}, \hat{C}_{\mathbf{k},\downarrow}, \hat{C}^\dagger_{-\mathbf{k},\downarrow}, -\hat{C}^\dagger_{-\mathbf{k},\uparrow}\right)^{\mathrm{T}}$ is the Nambu spinor and the photon-number dependent Bogoliubov-de-Gennes matrix is given by

$$\begin{aligned}\mathbf{M}_{\mathbf{k}} &= \begin{pmatrix} \xi_{\mathbf{k}} - \omega_0 & \bar{\eta} & \Delta & 0 \\ \bar{\eta} & \xi_{\mathbf{k}} + \omega_0 & 0 & \Delta \\ \Delta & 0 & -\xi_{\mathbf{k}} - \omega_0 & \bar{\eta} \\ 0 & \Delta & \bar{\eta} & -\xi_{\mathbf{k}} + \omega_0 \end{pmatrix} \\ &= \begin{pmatrix} H_0 & \Delta\mathbb{I} \\ \Delta\mathbb{I} & -\sigma_y H_0 \sigma_y \end{pmatrix},\end{aligned} \tag{3}$$

with $\bar{\eta} = \eta(\alpha + \alpha^*)/\sqrt{n}$, $H_0 = \xi_{\mathbf{k}} + \omega_0\sigma_z + \bar{\eta}\sigma_x$, the Pauli matrices σ_x and σ_y, and the 2×2 unit matrix $\mathbb{I}$. The property of the matrix (3) implies that the Hamiltonian (2) has the particle-hole symmetry. Diagonalizing the Hamiltonian (2) and considering the positive definition of the energies of the Bogoliubov quasiparticles with $E_{\mathbf{k},\pm} = \sqrt{\xi^2_{\mathbf{k}} + \Delta^2} \pm \sqrt{\bar{\eta}^2 + \omega_0^2}$, the ground-state energy is given by

$$\begin{aligned}E_{\mathrm{G}} = &\sum_{\mathbf{k}} E_{\mathbf{k},-}\Theta\left(-E_{\mathbf{k},-}\right) + \sum_{\mathbf{k}}\left(\xi_{\mathbf{k}} - \sqrt{\xi^2_{\mathbf{k}} + \Delta^2}\right) \\ &- \frac{\Delta^2}{\lambda} + \omega|\alpha|^2,\end{aligned} \tag{4}$$

where $\Theta(x)$ is the Heaviside step function. In terms of the gap equation $\partial E_{\mathrm{G}}/\partial\Delta = 0$, the particle number equation $\partial E_{\mathrm{G}}/\partial\mu = -n$, the SR equation $\partial E_{\mathrm{G}}/\partial|\alpha| = 0$, and the polarization equation $m = -\partial E_{\mathrm{G}}/\partial\omega_0$ [29], we have

$$\Delta\left[\sum_{\mathbf{k}}\frac{f(-E_{\mathbf{k},-})}{\sqrt{\xi^2_{\mathbf{k}} + \Delta^2}} - \sum_{\mathbf{k}}\frac{1}{\sqrt{\xi^2_{\mathbf{k}} + \Delta^2}} - \frac{2}{\lambda}\right] = 0, \tag{5}$$

$$\sum_{\mathbf{k}}\frac{\xi_{\mathbf{k}} f(-E_{\mathbf{k},-})}{\sqrt{\xi^2_{\mathbf{k}} + \Delta^2}} + \sum_{\mathbf{k}}\left(1 - \frac{\xi_{\mathbf{k}}}{\sqrt{\xi^2_{\mathbf{k}} + \Delta^2}}\right) = n, \tag{6}$$

$$|\alpha|\left[\sum_{\mathbf{k}} -2\omega\eta^2 f(-E_{\mathbf{k},-}) + n\bar{\chi}\left(\omega^2 + \kappa^2\right)\right] = 0, \tag{7}$$

$$\frac{\omega_0 f(-E_{\mathbf{k},-})}{\bar{\chi}} = m, \tag{8}$$

where $f(-E_{\mathbf{k},-}) = \Theta(-E_{\mathbf{k},-}) - E_{\mathbf{k},-}\delta(-E_{\mathbf{k},-})$ and $\bar{\chi} = \sqrt{\bar{\eta}^2 + \omega_0^2}$. Notice that when $k \to \infty$, eq. (5) diverges. In order to eliminate this ultraviolet divergence, λ should be renormalized as $1/\lambda = -\sum_{\mathbf{k}} 1/(2\epsilon_{\mathbf{k}} + E_{\mathrm{b}})$, where $E_{\mathrm{b}} > 0$ is the two-body binding energy in 2D [33, 34].

Finally, we self-consistently solve the coupled eqs. (5)-(8) at a fixed atom density n to obtain four parameters Δ, μ, $|\alpha|$, m, and then determine the ground state. For simplicity, in the following discussions we take E_{F} as the unit of energy and introduce the ground-state energy per fermion $\bar{E}_{\mathrm{G}} = E_{\mathrm{G}}/n$, the scaled mean-photon number $|\bar{\alpha}|^2 = |\alpha|^2/n$, and the scaled polarization $\bar{m} = m/n$.

4 Results

When both η and E_{b} exist, the properties of the Bogoliubov quasiparticle states are determined by both $\bar{\chi}$ and Δ. If $\bar{\chi} > \Delta$, the quasi-particle states are occupied for $\max\{0, \mu - \sqrt{\bar{\chi}^2 - \Delta^2}\} < \epsilon_{\mathbf{k}} < \mu + \sqrt{\bar{\chi}^2 - \Delta^2}$ ($\mu + \sqrt{\bar{\chi}^2 - \Delta^2} > 0$), and thus, the scaled ground-state energy is obtained by

$$\begin{aligned}\bar{E}_{\mathrm{G}} = &\bar{E}^{\mathrm{SF}}_{\mathrm{G}} + \omega|\bar{\alpha}|^2 - \frac{1}{4E_{\mathrm{F}}}\left[2\bar{\chi}\sqrt{\bar{\chi}^2 - \Delta^2}\right. \\ &\left.-\Delta^2\ln\left(\frac{\bar{\chi} + \sqrt{\bar{\chi}^2 - \Delta^2}}{\bar{\chi} - \sqrt{\bar{\chi}^2 - \Delta^2}}\right)\right]\Theta\left(\bar{\mu}_-\right)\Theta\left(\bar{\chi}^2 - \Delta^2\right) \\ &- \frac{1}{4E_{\mathrm{F}}}\left[\bar{\chi}\sqrt{\bar{\chi}^2 - \Delta^2} + \mu\left(2\bar{\chi} - \sqrt{\mu^2 + \Delta^2}\right)\right. \\ &\left.-\Delta^2\ln\left(-\frac{\bar{\chi} + \sqrt{\bar{\chi}^2 - \Delta^2}}{\mu - \sqrt{\mu^2 + \Delta^2}}\right)\right]\Theta\left(-\bar{\mu}_-\right)\Theta\left(\bar{\chi}^2 - \Delta^2\right),\end{aligned} \tag{9}$$

where $\bar{\mu}_- = \mu - \sqrt{\bar{\chi}^2 - \Delta^2}$ and

$$\begin{aligned}\bar{E}^{\mathrm{SF}}_{\mathrm{G}} = &\frac{\Delta^2}{4E_{\mathrm{F}}}\ln\left(\frac{\sqrt{\mu^2 + \Delta^2} - \mu}{E_{\mathrm{b}}}\right) \\ &- \frac{\mu}{4E_{\mathrm{F}}}\left(\sqrt{\mu^2 + \Delta^2} + \mu\right) - \frac{\Delta^2}{8E_{\mathrm{F}}}\end{aligned} \tag{10}$$

is the fully-paired ($\bar{m} = 0$) SF energy. If $\bar{\chi} < \Delta$, $\bar{E}_{\mathrm{G}} = \bar{E}^{\mathrm{SF}}_{\mathrm{G}}$. It can be seen clearly from eq. (9) that the ground-state properties, including Δ, μ, $|\bar{\alpha}|^2$, and $\bar{m}$, are governed by both η and E_{b}. When $E_{\mathrm{b}} = 0$, $\bar{\mu}_- = \mu - \bar{\chi}$ and $\bar{E}_{\mathrm{G}}$ is the same as eq. (29) in ref. [20]. When $E_{\mathrm{b}} \neq 0$ and $\eta \neq 0$, a strong competition

between the SF and SR properties occurs. Consequently, rich quantum phases can be predicted. Similarly, the Heaviside step function in eq. (9) depends crucially on $\bar{\mu}_-$ and $\bar{\chi}^2-\Delta^2$, and thus, the following discussions of the ground-state properties should also be divided into four specific cases: $\bar{\mu}_-<0$ and $\bar{\chi}^2-\Delta^2\geqslant 0$, $\bar{\mu}_-<0$ and $\bar{\chi}^2-\Delta^2<0$, $\bar{\mu}_-\geqslant 0$ and $\bar{\chi}^2-\Delta^2\geqslant 0$, and $\bar{\mu}_-\geqslant 0$ and $\bar{\chi}^2-\Delta^2<0$. Moreover, we will draw two conclusions for $\omega_0<E_{\rm F}$ and $\omega_0\geqslant E_{\rm F}$.

4.1 $\bar{\mu}_-<0$ and $\bar{\chi}^2-\Delta^2\geqslant 0$

When $\bar{\mu}_-<0$ and $\bar{\chi}^2-\Delta^2\geqslant 0$, eq. (9) becomes

$$\bar{E}_{\rm G}=\bar{E}_{\rm G}^{\rm SF}+\omega|\bar{\alpha}|^2+\frac{1}{4E_{\rm F}}\left[\Delta^2\ln\left(-\frac{\bar{\chi}+\sqrt{\bar{\chi}^2-\Delta^2}}{\mu-\sqrt{\mu^2+\Delta^2}}\right)-\bar{\chi}\sqrt{\bar{\chi}^2-\Delta^2}-\mu\left(2\bar{\chi}-\sqrt{\mu^2+\Delta^2}\right)\right]. \tag{11}$$

From eqs. (5)-(8), we obtain the following solutions:

$$\Delta=0,\quad \mu=2E_{\rm F}-\omega_0,\quad |\bar{\alpha}|=0,\ \bar{m}=1, \tag{12}$$

or

$$\Delta=0,\quad \mu=2\left(E_{\rm F}-\frac{\omega\eta^2}{\omega^2+\kappa^2}\right),\quad |\bar{\alpha}|=\sqrt{\frac{\eta^2}{\omega^2+\kappa^2}-\frac{\omega_0^2(\omega^2+\kappa^2)}{4\omega^2\eta^2}},\quad \bar{m}=\frac{\omega_0\left(\omega^2+\kappa^2\right)}{2\omega\eta^2}, \tag{13}$$

or

$$\Delta=\sqrt{E_{\rm b}(2\omega_0-E_{\rm b})},\ \mu=2E_{\rm F}-\omega_0,\quad |\bar{\alpha}|=0,\ \bar{m}=\frac{E_{\rm b}-2\omega_0+2E_{\rm F}}{2E_{\rm F}}, \tag{14}$$

or

$$\Delta=\sqrt{E_{\rm b}\left[\frac{2\omega\eta^2(2E_{\rm F}+E_{\rm b})}{2\omega\eta^2+(\omega^2+\kappa^2)E_{\rm F}}-E_{\rm b}\right]},\quad \mu=2E_{\rm F}-\frac{\omega\eta^2(2E_{\rm F}+E_{\rm b})}{2\omega\eta^2+(\omega^2+\kappa^2)E_{\rm F}},$$
$$|\bar{\alpha}|=\frac{\sqrt{(\omega^2+\kappa^2)}}{2}\sqrt{\left[\frac{\eta(2E_{\rm F}+E_{\rm b})}{2\omega\eta^2+(\omega^2+\kappa^2)E_{\rm F}}\right]^2-\frac{\omega_0^2}{\omega^2\eta^2}},\quad \bar{m}=\frac{\omega_0\left(\omega^2+\kappa^2\right)}{2\omega\eta^2}. \tag{15}$$

Since here the system has two dependent order parameters Δ and $|\bar{\alpha}|$, the ground-state stability should be determined by a 2×2 Hessian matrix [35], which is defined as:

$$\mathbf{M}=\begin{bmatrix}\dfrac{\partial^2\bar{E}_{\rm G}}{\partial\Delta^2} & \dfrac{\partial^2\bar{E}_{\rm G}}{\partial\Delta\partial|\bar{\alpha}|}\\ \dfrac{\partial^2\bar{E}_{\rm G}}{\partial|\bar{\alpha}|\partial\Delta} & \dfrac{\partial^2\bar{E}_{\rm G}}{\partial(|\bar{\alpha}|)^2}\end{bmatrix}. \tag{16}$$

If $\mathbf{M}$ is positive definite (i.e., two eigenvalues of $\mathbf{M}$ are positive), $\bar{E}_{\rm G}$ has local minima and the system is located at the stable phase. If $\mathbf{M}$ is indefinite (i.e., one eigenvalues is positive, while the other is negative), $\bar{E}_{\rm G}$ has saddle points and the system is dynamically unstable. If $\mathbf{M}$ is negative definite (i.e., two eigenvalues of $\mathbf{M}$ are negative), $\bar{E}_{\rm G}$ has a local maximum and the system is extremely unstable.

In terms of the stability condition given by eq. (16), the ground states corresponding to the solutions eq. (14) or eq. (15) are unstable, whereas for the solutions eq. (12) or eq. (13) they become stable. For $\Delta\equiv 0$ in both eqs. (12) and (13), using the stable condition governed by $\partial^2\bar{E}_{\rm G}/\partial(|\bar{\alpha}|)^2>0$, we can obtain the superradiant critical point $\eta_{\rm c}^{(1)}=\sqrt{\omega_0(\omega^2+\kappa^2)/(2\omega)}$ [20], which separates the solutions eqs. (12) and (13). In addition, the restrictive conditions in $\bar{\mu}_-<0$ and $\bar{\chi}^2-\Delta^2\geqslant 0$ lead to another critical point $\eta_{\rm c}^{(2)}=\sqrt{E_{\rm F}(\omega^2+\kappa^2)/(2\omega)}$ [20]. Comparing $\eta_{\rm c}^{(1)}$ with $\eta_{\rm c}^{(2)}$, we find that when $\omega_0\geqslant E_{\rm F}$, i.e., $\eta_{\rm c}^{(1)}>\eta_{\rm c}^{(2)}$, $\bar{\mu}_-<0$ and $\bar{\chi}^2-\Delta^2\geqslant 0$, and thus, for $0<\eta<\eta_{\rm c}^{(1)}$, Δ, μ, $|\bar{\alpha}|$, and $\bar{m}$ are governed by eq. (12), and for $\eta>\eta_{\rm c}^{(1)}$, they are governed by eq. (13). When $\omega_0<E_{\rm F}$, i.e., $\eta_{\rm c}^{(1)}<\eta_{\rm c}^{(2)}$, $\bar{\mu}_-\geqslant 0$ and $\bar{\chi}^2-\Delta^2\geqslant 0$, and thus, for $0<\eta<\eta_{\rm c}^{(2)}$, the scaled ground-state energy changes and we will discuss the relevant results in the following. However, for $\eta>\eta_{\rm c}^{(2)}$, $\bar{\mu}_-<0$ and $\bar{\chi}^2-\Delta^2\geqslant 0$, and thus, Δ, μ, $|\bar{\alpha}|$, and $\bar{m}$ are still governed by eq. (13).

4.2 $\bar{\mu}_-<0$ and $\bar{\chi}^2-\Delta^2<0$

When $\bar{\mu}_-<0$ and $\bar{\chi}^2-\Delta^2<0$, eq. (9) becomes

$$\bar{E}_{\rm G}=\bar{E}_{\rm G}^{\rm SF}+\omega|\bar{\alpha}|^2. \tag{17}$$

From eqs. (5)-(8), we obtain

$$\Delta=0,\ \mu=E_{\rm F},\quad |\bar{\alpha}|=0,\quad \bar{m}=0, \tag{18}$$

or

$$\Delta=\sqrt{2E_{\rm F}E_{\rm b}},\ \mu=E_{\rm F}-\frac{E_{\rm b}}{2},\ |\bar{\alpha}|=0,\ \bar{m}=0. \tag{19}$$

Since $|\bar{\alpha}|\equiv 0$ in eqs. (18) and (19), we can introduce the stable condition governed by $\partial^2\bar{E}_{\rm G}/\partial\Delta^2>0$ to find the stable ground state. According to this stable condition and $\bar{\mu}_-<0$ and $\bar{\chi}^2-\Delta^2<0$, we find that the ground state, with the solution (19), is stable for all $E_{\rm b}$ and η.

4.3 The ground state for cases 4.1 and 4.2

In terms of the above discussions in the sects. 4.1 and 4.2 of this section, we can obtain the stable ground-state properties for $\omega_0 \geqslant E_F$. In this case, there exist two kinds of competition governed by the solutions eqs. (12), (13) and (19). When $0 < \eta < \eta_c^{(1)}$, the solutions eqs. (12) and (19) dominate, whereas when $\eta > \eta_c^{(1)}$, the solutions eqs. (13) and (19) dominate. These solutions show two typical properties of the scaled ground-state energy. The first is that the scaled ground-state energy has a global minimum, i.e., the system is located at the normal phase featuring one Fermi surface (N-I), SF, or SR phases. The other is that the scaled ground-state energy has two degenerate minima, which implies that two of these phases can coexist. Thus, for $\omega_0 \geqslant E_F$, the results for the stable ground state are summarized as the following two situations: $0 < \eta < \eta_c^{(1)}$ and $\eta > \eta_c^{(1)}$.

4.3.1 $0 < \eta < \eta_c^{(1)}$

When $0 < \eta < \eta_c^{(1)}$, it can be seen from eqs. (12), (13) and (19) that the weak fermion-photon interaction has no effect on the systematic properties. In this case, only the N-I and SF phases can be found. More interestingly, when varying E_b, the ground-state energies for these two phases are equal, i.e., these two phases coexist and the corresponding phase is called the N-I-SF mixed phase.

From the phase equilibrium condition [29,30], we find that for $E_b < 2\left[\omega_0 - \left(\sqrt{2}-1\right)E_F\right]$, $\Delta = 0$, and $\bar{E}_G$, μ, and $\bar{m}$ are governed by

$$\bar{E}_G = -E_F, \quad \mu = 2E_F - \omega_0, \quad \bar{m} = 1. \tag{20}$$

This implies that the system is located at the N-I phase. For $2\left[\omega_0 - \left(\sqrt{2}-1\right)E_F\right] < E_b < 2\left[\omega_0 - \left(2-\sqrt{2}\right)E_F\right]$, we find $\bar{E}_G(\mu, \Delta \neq 0) = \bar{E}_G(\mu, \Delta = 0)$, which implies that the system is located at the N-I-SF mixed phase. In order to fully describe the fundamental properties of this mixed phase, we should introduce the fractions of the N-I and SF phases, x_1 and $1 - x_1$. Moreover, we further obtain

$$\bar{E}_G = \mu - \frac{x_1}{4E_F}\left(\frac{2\omega_0 - E_b}{2-\sqrt{2}}\right)^2 - \frac{1-x_1}{4E_F}\left(\frac{2\omega_0 - E_b}{2-\sqrt{2}}\right)^2, \tag{21}$$

$$\Delta = \sqrt{\frac{2\omega_0 E_b - E_b^2}{\sqrt{2}-1}}, \tag{22}$$

$$\mu = \frac{\sqrt{2}\omega_0 - E_b}{2-\sqrt{2}}, \tag{23}$$

$$\bar{m} = 1 - x_1, \tag{24}$$

where $x_1 = 2\sqrt{2}E_F/(2\omega_0 - E_b) - \sqrt{2} - 1$. For $E_b > 2\left[\omega_0 - \left(2-\sqrt{2}\right)E_F\right]$, we find

$$\bar{E}_G = -\frac{E_F}{2}, \ \Delta = \sqrt{2E_F E_b}, \ \mu = E_F - \frac{E_b}{2}, \ \bar{m} = 0, \tag{25}$$

which indicates that the system is located at the SF phase. The analytical results in eqs. (20)-(25) are the same as those in refs. [30,36], as expected. They show that when increasing E_b, two first-order phase transitions from the N-I phase to the N-I-SF mixed phase or from the N-I-SF mixed phase to the SF phase emerge [29, 30, 32, 36-38]. Moreover, the ratio of the scaled polarization to the dimensionless mean-field gap in the N-II-SF mixed phase, $\bar{m}/(\Delta/E_F)$, is decreased.

4.3.2 $\eta > \eta_c^{(1)}$

When $\eta > \eta_c^{(1)}$, it can be seen from eq. (13) that a non-zero $|\bar{\alpha}|$ emerges, which means that the fermion-photon interaction has a significant effect on the systematic properties. In this case, only the SF and SR phases can be found. More interestingly, when varying E_b and η, the ground-state energies for these two phases are equal, i.e., these two phases coexist and the corresponding phase is called the SF-SR mixed phase.

From the phase equilibrium condition [29,30], we find four stable regions as follows.

(i) When $E_b < E_b^{(1)}$, $\Delta = 0$, and $\bar{E}_G$, μ, $|\bar{\alpha}|$, and $\bar{m}$ are governed by eqs. (38)-(41) in ref. [20]. These mean that the system is located at the SR phase.

(ii) When $E_b^{(1)}\Theta\left(\eta_c^{(3)} - \eta\right) < E_b < 2\left[\omega_0 - \left(2-\sqrt{2}\right)E_F\right] \cdot \Theta\left(\eta_c^{(3)} - \eta\right)$ or $E_b^{(2)}\Theta\left(\eta - \eta_c^{(3)}\right) < E_b < 2\left[\omega_0 - \left(2-\sqrt{2}\right)E_F\right] \cdot \Theta\left(\eta - \eta_c^{(3)}\right)$, with $\eta_c^{(3)} = \omega_0\sqrt{(\omega^2+\kappa^2)/2\omega}$, we find $\bar{E}_G(\mu, \Delta \neq 0, |\bar{\alpha}| = 0) = \bar{E}_G(\mu, \Delta = 0, |\bar{\alpha}| = 0)$, which means that the N-I and SF phases coexist and the corresponding phase is called the N-I-SF mixed phase. We further obtain $\bar{E}_G$, Δ, μ, and $\bar{m}$, which are governed by eqs. (21)-(24).

(iii) When $E_b^{(1)} < E_b < E_b^{(2)}\Theta\left(\eta - \eta_c^{(3)}\right)$, we find $\bar{E}_G(\mu, \Delta \neq 0, |\bar{\alpha}| = 0) = \bar{E}_G(\mu, \Delta = 0, |\bar{\alpha}| \neq 0)$, which implies that the system is located at the SF-SR mixed phase. In order to fully describe the fundamental properties of this mixed phase, we should introduce the fractions of the SF and SR phases, x_2 and $1 - x_2$. Moreover, we further obtain

$$\bar{E}_G = \mu - x_2\frac{1}{2E_F}\left(\mu + \frac{E_b}{2}\right)^2 - (1-x_2)\left[\frac{\mu^2}{4E_F A} + \frac{\omega_0^2\left(\omega^2+\kappa^2\right)}{4\omega\eta^2}\right], \tag{26}$$

$$\Delta = \sqrt{E_b(E_b + 2\mu)}, \tag{27}$$

$$\mu = \frac{-E_b A \pm \sqrt{A^2E_b^2 - 2A(2A-1)B}}{2A-1}, \tag{28}$$

$$|\bar{\alpha}| = \frac{1}{2}\sqrt{\frac{\mu^2\eta^2}{(\omega^2+\kappa^2)E_F^2A^2} - \frac{\omega_0^2(\omega^2+\kappa^2)}{\omega^2\eta^2}}, \tag{29}$$

$$\bar{m} = (1-x_2)\frac{\omega_0\left(\omega^2+\kappa^2\right)}{2\omega\eta^2}, \tag{30}$$

where $A = 1 - \omega\eta^2/\left[E_{\mathrm{F}}\left(\omega^2+\kappa^2\right)\right]$, $B = E_{\mathrm{b}}^2/4 - E_{\mathrm{F}}\omega_0^2\left(\omega^2+\kappa^2\right)/\left(2\omega\eta^2\right)$, and $x_2 = (2E_{\mathrm{F}}A-\mu)/(2\mu A-\mu+E_{\mathrm{b}}A)$. In principle, $E_{\mathrm{b}}^{(1)}$ and $E_{\mathrm{b}}^{(2)}$ can be obtained analytically. However, their expressions are so complicated that here we do not list them.

Finally, we prove that the SF-SR mixed phase has a lowest scaled ground-state energy. The scaled ground-state energy in the SF-SR mixed phase is defined as [29, 30]:

$$\bar{E}_{\mathrm{G}}^{\text{SF-SR}}(\omega_0, E_{\mathrm{b}}, \eta) = \mu + x_2\bar{E}_{\mathrm{G}}^{\mathrm{SF}}(\mu, E_{\mathrm{b}}) + (1-x_2)\bar{E}_{\mathrm{G}}^{\mathrm{SR}}(\mu, \eta). \tag{31}$$

The differences between $\bar{E}_{\mathrm{G}}^{\text{SF-SR}}(\omega_0, E_{\mathrm{b}}, \eta)$ and $\bar{E}_{\mathrm{G}}^{\mathrm{SF}}(\omega_0, E_{\mathrm{b}}, \eta)$ or between $\bar{E}_{\mathrm{G}}^{\text{SF-SR}}(\omega_0, E_{\mathrm{b}}, \eta)$ and $\bar{E}_{\mathrm{G}}^{\mathrm{SR}}(\omega_0, E_{\mathrm{b}}, \eta)$ are given by

$$\bar{E}_{\mathrm{G}}^{\text{SF-SR}}(\omega_0, E_{\mathrm{b}}, \eta) - \bar{E}_{\mathrm{G}}^{\mathrm{SF}}(\omega_0, E_{\mathrm{b}}, \eta) = -\frac{1}{2E_{\mathrm{F}}}\left(\frac{\mu^2}{2A}+E_{\mathrm{F}}^2-E_{\mathrm{F}}E_{\mathrm{b}}\right)+\mu-\frac{\omega_0^2\left(\omega^2+\kappa^2\right)}{4\omega\eta^2}, \tag{32}$$

$$\bar{E}_{\mathrm{G}}^{\text{SF-SR}}(\omega_0, E_{\mathrm{b}}, \eta) - \bar{E}_{\mathrm{G}}^{\mathrm{SR}}(\omega_0, E_{\mathrm{b}}, \eta) = -E_{\mathrm{F}}+\mu-\frac{\mu^2}{4E_{\mathrm{F}}A}+\frac{\omega\eta^2}{\omega^2+\kappa^2}. \tag{33}$$

It can be seen clearly from eqs. (28), (32) and (33) that these energy differences are negative, i.e., the SF-SR mixed phase has a lowest scaled ground-state energy for $E_{\mathrm{b}}^{(1)} < E_{\mathrm{b}} < E_{\mathrm{b}}^{(2)}\left(\eta-\eta_{\mathrm{c}}^{(3)}\right)$.

The analytical results in eqs. (27)-(30) show that the predicted SF-SR mixed phase has the following typical properties:

• When $x_2 = 0$, the system is located at the SR phase with $\bar{m} = \omega_0\left(\omega^2+\kappa^2\right)/\left(2\omega\eta^2\right)$, whereas when $x_2 = 1$, the system enters into the SF phase with $\bar{m} = 0$. The above explicit expressions show that the nonzero $\bar{m}$ in the SF-SR mixed phase is only caused by the macroscopic collective excitation of both the fermions and photons, which is different from that of the N-I-SF phase.

• For a relative small E_{b} or larger η, $x_2 \to 0$, as shown in Figure 2. This means that the systematic property is mainly governed by the SR property. Whenever increasing η or E_{b}, $\bar{m}$ is decreased, and Δ and $|\bar{\alpha}|$ are increased, as shown in Figure 3(a)-(c).

• For a relative small η or larger E_{b}, $x_2 \to 1$, as also shown in Figure 2. This means that the systematic property is mainly governed by the SF property. In this case, $\bar{m}$ approaches zero, as also shown in Figure 3(a), and Δ and $|\bar{\alpha}|$ almost reach their maximum values, as also shown in Figure 3(b) and (c).

• For the intermediate η and E_{b}, both x_2 and $1-x_2$ are the finite values ranging from 0 to 1, as also shown in Figure 2. These mean that the SF and SR properties have a strong competition. When increasing E_{b}, $\bar{m}$ is decreased, and thus, both Δ and $|\bar{\alpha}|$ are increased, as also shown in Figure 3(a)-(c). However, when increasing η, $\bar{m}$ is increased, due to the rapid increasing of $1-x_2$, i.e., the fraction of the SR phase, and thus, both Δ and $|\bar{\alpha}|$ are decreased, as also shown in Figure 3(a)-(c). This is quite different from that in the SR phase, in which when increasing η, $\bar{m}$ is decreased. In order to see clearly the evolution of $\bar{m}$ and Δ, we plot $\bar{m}/(\Delta/E_{\mathrm{F}})$ as a function of η and E_{b} in Figure 4. For a fixed E_{b}, when increasing η, $\bar{m}/(\Delta/E_{\mathrm{F}})$ is increased, as shown in Figure 4(a) and (b). Based on this conclusion, we expect that in real experiments we can tune η and E_{b} to find a relative large regime that the magnetic and SF properties coexist. This is also different from the situation in the N-II-SF mixed phase, in which when increasing E_{b} the coexisted regime becomes smaller

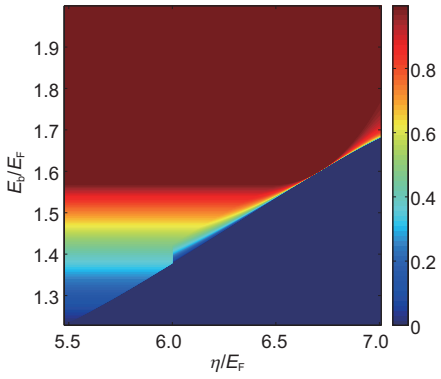

Figure 2 (Color online) The fraction of the SF phase, x_2, as a function of the two-body binding energy $E_{\mathrm{b}}/E_{\mathrm{F}}$ and the effective fermion-photon coupling strength η/E_{F}, when the effective resonant frequency is chosen as $\omega_0 = 1.2E_{\mathrm{F}}$. The atom-number dependent cavity frequency and the cavity decay rate are given by $\omega = 10E_{\mathrm{F}}$ and $\kappa = 20E_{\mathrm{F}}$, respectively.

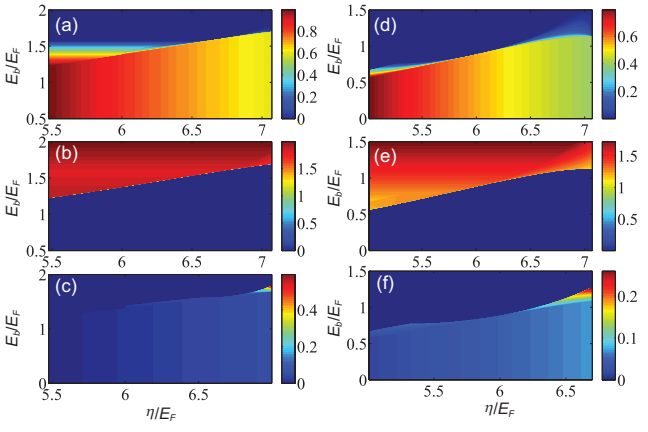

Figure 3 (Color online) (a), (d) The scaled polarization $\bar{m}$; (b), (e) the mean-field gap Δ/E_{F}; and (c), (f) the scaled mean-photon number $|\bar{\alpha}|^2$ as functions of the two-body binding energy $E_{\mathrm{b}}/E_{\mathrm{F}}$ and the effective fermion-photon coupling strength η/E_{F}, when the effective resonant frequency is chosen as $\omega_0 = 1.2E_{\mathrm{F}}$ ((a)-(c)) or $\omega_0 = 0.8E_{\mathrm{F}}$ ((d)-(f)). The atom-number dependent cavity frequency ω and the cavity decay rate κ are the same as those in Figure 2.

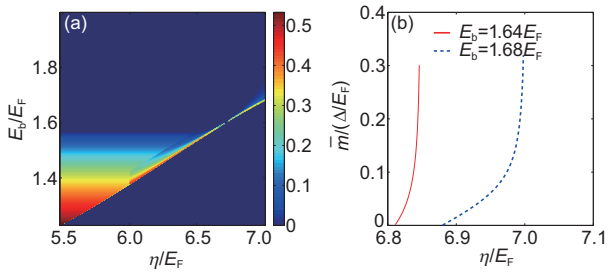

Figure 4 (Color online) (a) The ratio of the scaled polarization to the dimensionless mean-field gap in the N-I-SF mixed state, $\bar{m}/(\Delta/E_{\rm F})$, as a function of the two-body binding energy $E_{\rm b}/E_{\rm F}$ and the effective fermion-photon coupling strength $\eta/E_{\rm F}$, when the effective resonant frequency is chosen as $\omega_0 = 1.2E_{\rm F}$. The atom-number dependent cavity frequency ω and the cavity decay rate κ are the same as those in Figure 2(b) For a fixed $E_{\rm b} = 1.64E_{\rm F}$ (the red-solid line) and $E_{\rm b} = 1.68E_{\rm F}$ (the blue-dashed line), $\bar{m}/(\Delta/E_{\rm F})$ varies as a function of $\eta/E_{\rm F}$.

and smaller. In addition, $\bar{m}/|\bar{\alpha}|$ has a similar behavior, and thus, is not addressed here.

(iv) When $E_{\rm b} > 2\left[\omega_0 - \left(2-\sqrt{2}\right)E_{\rm F}\right]\Theta\left(\eta_{\rm c}^{(3)} - \eta\right)$ or $E_{\rm b} > E_{\rm b}^{(2)}\Theta\left(\eta - \eta_{\rm c}^{(3)}\right)$, $|\bar{\alpha}| = 0$, and $\bar{E}_{\rm G}$, Δ, μ, and $\bar{m}$ are governed by eq. (25). These mean that the system is located at the SF phase.

4.3.3 *Phase diagram*

In Figure 5(a), we plot the whole phase diagram, including the N-I phase, the N-I-SR mixed phase, the SF-SR mixed phase, the SF phase, and the SR phase, for $0 < \eta < \eta_{\rm c}^{(1)}$ and $\eta > \eta_{\rm c}^{(1)}$. The phase transitions, from the N-I-SF mixed phase to the N-I phase or the SF phase or the SR phase or the SF-SR mixed phase and from the SF-SR mixed phase to the SF phase or the SP phase, are of the first order, due to the existence of the N-I-SF and SF-SR mixed phases. However, the phase transition from the N-I phase to the SR phase is of the second order. In addition, this phase diagram has a tricritical point (the green dot), at which the phase transition changes from the first order to the second order.

4.4 $\bar{\mu}_- \geqslant 0$ and $\bar{\chi}^2 - \Delta^2 \geqslant 0$

When $\bar{\mu}_- \geqslant 0$ and $\bar{\chi}^2 - \Delta^2 \geqslant 0$, the scaled ground-state energy in eq. (9) becomes

$$\bar{E}_{\rm G} = \bar{E}_{\rm G}^{\rm SF} + \omega|\bar{\alpha}|^2 - \frac{\bar{\chi}}{2E_{\rm F}}\sqrt{\bar{\chi}^2-\Delta^2} - \frac{\Delta^2}{4E_{\rm F}}\ln\left(\frac{\bar{\chi}+\sqrt{\bar{\chi}^2-\Delta^2}}{\bar{\chi}-\sqrt{\bar{\chi}^2-\Delta^2}}\right). \tag{34}$$

From eqs. (5)-(8), we obtain the following solutions:

$$\Delta = 0,\ \mu = E_{\rm F},\ |\bar{\alpha}| = 0,\ \bar{m} = \frac{\omega_0}{E_{\rm F}}, \tag{35}$$

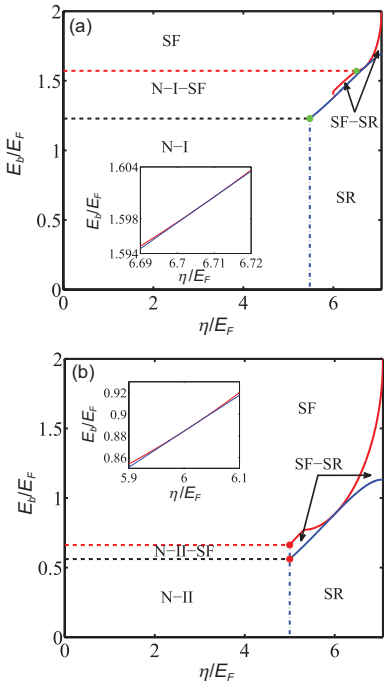

Figure 5 (Color online) Phase diagrams as a function of the two-body binding energy $E_{\rm b}/E_{\rm F}$ and the effective atom-photon coupling strength $\eta/E_{\rm F}$ for different effective resonant frequency. The effective resonant frequency is chosen as (a) $\omega_0 = 1.2E_{\rm F}$ and (b) $\omega_0 = 0.8E_{\rm F}$, respectively. The atom-number dependent cavity frequency ω and the cavity decay rate κ are also the same as in Figure 2. Inset: the region of the phase boundaries approaching each other.

or

$$\Delta = \sqrt{\sqrt{2E_{\rm F}E_{\rm b}}\left(2\omega_0 - \sqrt{2E_{\rm F}E_{\rm b}}\right)},$$
$$\mu = E_{\rm F} + \frac{E_{\rm b}}{2} - \frac{\omega_0\sqrt{2E_{\rm F}E_{\rm b}}}{2E_{\rm F}}, \tag{36}$$
$$|\bar{\alpha}| = 0,\ \bar{m} = \frac{\sqrt{\omega_0^2 - \sqrt{2E_{\rm F}E_{\rm b}}\left(2\omega_0 - \sqrt{2E_{\rm F}E_{\rm b}}\right)}}{E_{\rm F}},$$

or

$$\Delta = \sqrt{2E_{\rm F}E_{\rm b}}\sqrt{\frac{2\omega\eta^2 - E_{\rm F}(\omega^2+\kappa^2)}{2\omega\eta^2 + E_{\rm F}(\omega^2+\kappa^2)}},$$
$$\mu = E_{\rm F} + \frac{E_{\rm b}}{2} - \frac{2\omega\eta^2 E_{\rm b}}{2\omega\eta^2 + E_{\rm F}(\omega^2+\kappa^2)}, \tag{37}$$
$$|\bar{\alpha}| = \sqrt{\frac{2\eta^2 E_{\rm F}E_{\rm b}(\omega^2+\kappa^2)}{\left[2\omega\eta^2 + E_{\rm F}(\omega^2+\kappa^2)\right]^2} - \frac{\omega_0^2(\omega^2+\kappa^2)}{4\omega^2\eta^2}},$$
$$\bar{m} = \frac{\omega_0\left(\omega^2+\kappa^2\right)}{2\omega\eta^2}.$$

In terms of the stability condition given by eq. (16), the ground states corresponding to the solutions (36) and (37) are unstable, whereas for the solution (35) it becomes stable. For $\Delta \equiv 0$ using the stable condition governed by $\partial^2\bar{E}_{\rm G}/\partial(|\bar{\alpha}|)^2 > 0$ and the restrictive conditions $\bar{\mu}_- \geqslant 0$ and

$\bar{\chi}^2 - \Delta^2 \geqslant 0$, we find that when $\omega_0 < E_F$, $\bar{\mu}_- \geqslant 0$ and $\bar{\chi}^2 - \Delta^2 \geqslant 0$, and thus, for $0 < \eta < \eta_c^{(2)}$, Δ, μ, $|\bar{\alpha}|$, and $\bar{m}$ are governed by eq. (35), whereas for $\eta > \eta_c^{(2)}$, $\bar{\mu}_- < 0$ and $\bar{\chi}^2 - \Delta^2 \geqslant 0$, we should combine with the previous discussions in the case of $\bar{\mu}_- < 0$ and $\bar{\chi}^2 - \Delta^2 \geqslant 0$, and thus, Δ, μ, $|\bar{\alpha}|$, and $\bar{m}$ are governed by eq. (13).

4.5 $\bar{\mu}_- \geqslant 0$ and $\bar{\chi}^2 - \Delta^2 < 0$

Finally, when $\bar{\mu}_- \geqslant 0$ and $\bar{\chi}^2 - \Delta^2 < 0$, $\bar{E}_G$ in eq. (9) becomes

$$\bar{E}_G = \bar{E}_G^{SF} + \omega |\bar{\alpha}|^2 , \tag{38}$$

which is the same as eq. (17). Thus, the stable ground-state properties are the same with those in the case of $\bar{\mu}_- < 0$ and $\bar{\chi}^2 - \Delta^2 < 0$.

4.6 The ground state for cases 4.1, 4.4, and 4.5

In terms of the above discussions in the sects. 4.1, 4.4 and 4.5 of this section, we can obtain the stable ground-state properties for $\omega_0 < E_F$. In this case, there also exist two kinds of competition governed by the solutions (13), (19), and (35). When $0 < \eta < \eta_c^{(2)}$, the solutions (19) and (35) dominate, whereas when $\eta > \eta_c^{(2)}$, the solutions (13) and (19) dominate. These solutions also show two typical properties of the scaled ground-state energy. The first is that the scaled ground-state energy has a global minimum, i.e., the system is located at the normal phase featuring two Fermi surfaces (N-II), SF, and SR phases. The other is that the scaled ground-state energy has two degenerate minima, which implies that two of these phases can coexist. Thus, for $\omega_0 < E_F$, the results for the stable ground state are also summarized as the following two situations: $0 < \eta < \eta_c^{(2)}$ and $\eta > \eta_c^{(2)}$.

4.6.1 $0 < \eta < \eta_c^{(2)}$

When $0 < \eta < \eta_c^{(2)}$, it can be seen from eqs. (13), (19) and (35) that the weak fermion-photon interaction has no effect on the systematic properties. In this case, only the N-II and SF phases can be found. More interestingly, when varying E_b, the ground-state energies for these two phases are equal, i.e., these two phases coexist and the corresponding phase is called the N-II-SF mixed phase.

From the phase equilibrium condition [29,30], we find that for $E_b < 2\left(\sqrt{E_F^2 + \omega_0^2} - E_F\right)$, $\Delta = 0$, and $\bar{E}_G$, μ, and $\bar{m}$ are governed by

$$\bar{E}_G = -\frac{E_F}{2} - \frac{\omega_0^2}{2E_F}, \ \mu = E_F, \ \ \bar{m} = \frac{\omega_0}{E_F}. \tag{39}$$

This implies that the system is located at the N-II phase. For $2\left(\sqrt{E_F^2 + \omega_0^2} - E_F\right) < E_b < 2\left(E_F - \sqrt{E_F^2 - \omega_0^2}\right)\Theta(\omega_0 - \omega_{01})$, where $\omega_{01} = E_b\left(1 + \sqrt{2}\right)/2$ is determined by $\mu_{c1} = \omega_0$, we find $\bar{E}_G(\mu, \Delta = 0) = \bar{E}_G(\mu, \Delta \neq 0)$. This implies that the system is located at the N-II-SF mixed phase. In order to fully describe the fundamental properties of this mixed phase, we should introduce the fractions of the N-II and SF phases, x_3 and $1 - x_3$. Moreover, we further obtain

$$\bar{E}_G = \mu - \frac{x_3}{2E_F}\left(\frac{\omega_0^2}{E_b} + \frac{E_b}{4}\right)^2 - (1 - x_3)\frac{\left(4\omega_0^2 + E_b^2\right)^2}{32E_F E_b^2}, \tag{40}$$

$$\Delta = \sqrt{\frac{E_b^2 + 4\omega_0^2}{2}}, \tag{41}$$

$$\mu = \frac{\omega_0^2}{E_b} - \frac{E_b}{4}, \tag{42}$$

$$\bar{m} = (1 - x_3)\frac{\omega_0}{E_F}, \tag{43}$$

where $x_3 = 1/2 + 2E_F/E_b - 2\omega_0^2/E_b^2$. For $E_b > 2\left(E_F - \sqrt{E_F^2 - \omega_0^2}\right)\Theta(\omega_{01} - \omega_0)$, we find that $\bar{E}_G$, Δ, μ, and $\bar{m}$ are governed by eq. (25), which also indicates that the system is located at the SF phase. The analytical results in eqs. (39), (25), and (40)-(43) are also the same as those in refs. [30, 36], as expected. The basic properties of the N-II-SF mixed phase are similar to those in the N-I-SF mixed phase, and thus, are not discussed here.

4.6.2 $\eta > \eta_c^{(2)}$

When $\eta > \eta_c^{(2)}$, it can be seen from eq. (13) that the fermion-photon interaction plays a significant role in the systematic properties, which are sharply in contrast to the case of $0 < \eta < \eta_c^{(2)}$ and similar to the case of $\eta > \eta_c^{(1)}$ discussed above. In terms of eqs. (13) and (19), we plot Δ, μ, $|\bar{\alpha}|$, and $\bar{m}$ as functions of E_b and η in Figure 3(d)-(f), and find three stable regions as follows.

(i) When $E_b < E_b^{(1)}$, $\Delta = 0$, and $\bar{E}_G$, μ, $|\bar{\alpha}|$, and $\bar{m}$ are governed by eqs. (44) and (39)-(41) in ref. [20]. These mean that the system is located at the SR phase.

(ii) When $E_b^{(1)} < E_b < E_b^{(2)}$, we find $\bar{E}_G(\mu, \Delta \neq 0, |\bar{\alpha}| = 0) = \bar{E}_G(\mu, \Delta = 0\ |\bar{\alpha}| \neq 0)$, which means that the SF and SR phases coexist and the corresponding phase is called the SF-SR mixed phase. We further obtain $\bar{E}_G$, Δ, μ, $|\bar{\alpha}|$, and $\bar{m}$, which are governed by eqs. (26)-(30). The other typical properties in this SF-SR mixed phase are the same as those in the region of $\eta \geqslant \eta_c^{(1)}$, and thus, are not addressed here.

(iii) When $E_b > E_b^{(2)}$, $|\bar{\alpha}| = 0$, and $\bar{E}_G$, Δ, μ, and $\bar{m}$ are governed by eq. (25). These mean that the system is located at the SF phase.

4.6.3 Phase diagram

In Figure 5(b), we plot the whole phase diagram, including the N-II phase, the N-II-SR mixed phase, the SF-SR mixed

phase, the SF phase, and the SR phase, for $0 < \eta < \eta_c^{(2)}$ and $\eta > \eta_c^{(2)}$. All the phase transitions are of the first order, due to the existence of the N-II-SR and SF-SR mixed phases.

5 Parameter estimation and possible experimental observation

We now estimate the parameters of ^{40}K atoms for experiments. The ground-states $|\uparrow\rangle$ and $|\downarrow\rangle$ correspond to the states $|F = 9/2, m_F = 9/2\rangle$ and $|F = 9/2, m_F = 7/2\rangle$, respectively. As we discussed in ref. [20], we consider the optical properties of the ^{40}K D1-line. The corresponding cavity length is taken as 178 μm and the wavelengths of the transverse pumping lasers is taken as 770 nm. Therefore, the fermion-photon coupling strength g_1 and g_2 are at the order of MHz. The decay rate κ is estimated at the order of MHz under a waist radius 27 μm and a finesse $\sim 10^5$ for a cavity. Due to the prefactor $\sqrt{n}$, the effective fermion-photon coupling strength η is at the order of MHz. Finally, in the experiments [4], both the effective resonant frequency ω_0 and the atom-number dependent cavity frequency ω can be tuned from −GHz to GHz and even beyond. In addition, the 2D degenerate Fermi gas has been realized experimentally by a 1D deep optical lattice along the third dimension, where the tunneling between different layers is suppressed completely [39]. The 1D optical lattice potential $V_0 \sin^2(2\pi x/\lambda_w)$ can be generated using two counter-propagating laser beams (parallel to the x axis with wavelength λ_w). In this case, $E_b \simeq 0.915\hbar\omega_L \exp(\sqrt{2\pi} l_L/a_s)/\pi$, where $\omega_L = \sqrt{8\pi^2 V_0/(m\lambda_w^2)}$ is the effective trapping frequency along the x axis, $l_L = \sqrt{\hbar/(m\omega_L)}$, and a_s is the 3D s-wave scattering length [40]. Therefore, E_b can be tuned by varying the 3D s-wave scattering length a_s via the Feshbash resonance and can reach the order of MHz [22]. Based on the above estimation, all parameters used to plot Figures 2-5 could be realized in experiments.

Finally, we address the detection of the predicted quantum phases and phase diagrams briefly. From the above analysis, it is clearly that the properties of the ground-state is mainly determined by the mean-field gap Δ, the scaled mean-photon number $|\bar{\alpha}|^2$, and the scaled polarization $\bar{m}$. In experiments, the mean-field gap can be measured by the radio-frequency excitation spectra, i.e., the fractional loss of the fermions in one of the lowest substates through varying the radio-frequency frequency [41], $\bar{m}$ and the properties of the mixed phase can be measured by observing the different density distributions between the two-component Fermi gas [37, 38], and $|\alpha|^2$ can be detected using calibrated single-photon counting modules, which allow us to monitor the intracavity light intensity *in situ* [4]. Based on the latest state of the art experimental techniques, we expect that our predicted quantum phases and phase diagrams could be detected in future experiments.

6 Discussion and conclusion

In experiments, the Fermi gases are loaded in a 2D harmonic trap inside an optical cavity. The effects of the harmonic trap are taken into account using the local density approximation, as shown in ref. [20].

In summary, we have analytically investigated the ground-state properties of the interacting degenerate Fermi gas inside a cavity. We have found rich quantum phases and phase diagrams, which depend crucially on the fermion-photon coupling strength, the fermion-fermion interaction strength, and the atomic resonant frequency (effective Zeeman field). In particular, with the intermediate fermion-fermion interaction and fermion-photon coupling strengths, we have predicted new mixed phase with both the SF and SR properties. Moreover, in this mixed phase a relatively large ratio of the scaled polarization to the dimensionless mean-field gap, which is in contrast to that in the conventional superfluid regime can be obtained. Finally, we have presented a parameter estimation and have addressed briefly how to detect these predicted quantum phases and phase diagrams in experiments.

This work is supported by the National Key R&D Program of China (Grant No. 2017YFA0304203), the National Natural Science Foundation of China (NSFC) (Grant Nos. 11674200, 11422433, 11604392, 11434007, and 61378049), the Changjiang Scholars and Innovative Research Team in University of Ministry of Education of China (PCSIRT) (Grant No. IRT13076), the Foundation for the Author of National Excellent Doctoral Dissertation of China (FANEDD) (Grant No. 201316), and the Fund for Shanxi "1331 Project" Key Subjects Construction.

1 H. Ritsch, P. Domokos, F. Brennecke, and T. Esslinger, Rev. Mod. Phys. **85**, 553 (2013), arXiv: 1210.0013.
2 Y. K. Wang, and F. T. Hioe, Phys. Rev. A **7**, 831 (1973).
3 F. T. Hioe, Phys. Rev. A **8**, 1440 (1973).
4 K. Baumann, C. Guerlin, F. Brennecke, and T. Esslinger, Nature **464**, 1301 (2010), arXiv: 0912.3261.
5 K. Baumann, R. Mottl, F. Brennecke, and T. Esslinger, Phys. Rev. Lett. **107**, 140402 (2011), arXiv: 1105.0426.
6 M. P. Baden, K. J. Arnold, A. L. Grimsmo, S. Parkins, and M. D. Barrett, Phys. Rev. Lett. **113**, 020408 (2014), arXiv: 1404.0512.
7 Z. L. Xiang, T. Yu, W. X. Zhang, X. D. Hu, and J. Q. You, Sci. China-Phys. Mech. Astron. **55**, 1549 (2012), arXiv: 1208.5539.
8 Y. M. Liu, and R. W. Liu, Sci. China-Phys. Mech. Astron. **57**, 2259 (2014).
9 R. Kanamoto, and P. Meystre, Phys. Rev. Lett. **104**, 063601 (2010), arXiv: 0911.4748.
10 Q. Sun, X. H. Hu, A. C. Ji, and W. M. Liu, Phys. Rev. A **83**, 043606 (2011).
11 B. Padhi, and S. Ghosh, Phys. Rev. Lett. **111**, 043603 (2013).

12 J. Keeling, M. J. Bhaseen, and B. D. Simons, Phys. Rev. Lett. **112**, 143002 (2014), arXiv: 1309.2464.
13 F. Piazza, and P. Strack, Phys. Rev. Lett. **112**, 143003 (2014).
14 Y. Chen, Z. Yu, and H. Zhai, Phys. Rev. Lett. **112**, 143004 (2014), arXiv: 1309.3784.
15 J. S. Pan, X. J. Liu, W. Zhang, W. Yi, and G. C. Guo, Phys. Rev. Lett. **115**, 045303 (2015), arXiv: 1410.8431.
16 A. Sheikhan, F. Brennecke, and C. Kollath, Phys. Rev. A **93**, 043609 (2016), arXiv: 1602.01723.
17 A. Sheikhan, F. Brennecke, and C. Kollath, Phys. Rev. A **94**, 061603(R) (2016), arXiv: 1611.08463.
18 F. Mivehvar, H. Ritsch, and F. Piazza, Phys. Rev. Lett. **118**, 073602 (2017), arXiv: 1611.04876.
19 C. Kollath, A. Sheikhan, S. Wolff, and F. Brennecke, Phys. Rev. Lett. **116**, 060401 (2016), arXiv: 1502.01817.
20 Y. Feng, K. Zhang, J. Fan, F. Mei, G. Chen, and S. Jia, Sci. Rep. **7**, 10568 (2017), arXiv: 1701.02897.
21 S. Giorgini, L. P. Pitaevskii, and S. Stringari, Rev. Mod. Phys. **80**, 1215 (2008), arXiv: 0706.3360.
22 C. Chin, R. Grimm, P. Julienne, and E. Tiesinga, Rev. Mod. Phys. **82**, 1225 (2010).
23 K. J. Jiang, H. Luo, K. Li, D. F. Zhang, T. Y. Gao, and S. G. Peng, Sci. China-Phys. Mech. Astron. **56**, 581 (2013).
24 W. Yi, W. Zhang, and X. L. Cui, Sci. China-Phys. Mech. Astron. **58**, 014201 (2015), arXiv: 1410.1595.
25 J. K. Wang, J. G. Chen, K. J. Chen, W. Yi, and W. Zhang, Sci. China-Phys. Mech. Astron. **59**, 693011 (2016).
26 L. H. Zhou, W. Yi, and X. L. Cui, Sci. China-Phys. Mech. Astron. **60**, 127011 (2017).
27 Y. Chen, H. Zhai, and Z. Yu, Phys. Rev. A **91**, 021602 (2015), arXiv: 1411.0429.
28 D. Yu, J. S. Pan, X. J. Liu, W. Zhang, and W. Yi, Front. Phys. **13**, 136701 (2018).
29 D. E. Sheehy, and L. Radzihovsky, Ann. Phys. **322**, 1790 (2007).
30 L. He, and P. Zhuang, Phys. Rev. A **78**, 033613 (2008), arXiv: 0801.3127.
31 J. Du, C. Chen, and J. Liang, Phys. Rev. A **80**, 023601 (2009).
32 H. Caldas, A. L. Mota, R. L. S. Farias, and L. A. Souza, J. Stat. Mech. **2012**, P10019 (2012), arXiv: 1108.5407.
33 M. Randeria, J. M. Duan, and L. Y. Shieh, Phys. Rev. Lett. **62**, 981 (1989).
34 M. Randeria, J. M. Duan, and L. Y. Shieh, Phys. Rev. B **41**, 327 (1990).
35 S. Bell, J. S. Crighton, and R. Fletcher, Chem. Phys. Lett. **82**, 122 (1981).
36 D. E. Sheehy, Phys. Rev. A **92**, 053631 (2015), arXiv: 1407.8021.
37 G. B. Partridge, Science **311**, 503 (2006).
38 M. W. Zwierlein, Science **311**, 492 (2006).
39 M. Koschorreck, D. Pertot, E. Vogt, B. Fröhlich, M. Feld, and M. Köhl, Nature **485**, 619 (2012), arXiv: 1203.1009.
40 J. Levinsen, and M. M. Parish, in *Annual Review of Cold Atoms and Molecules,* Volume 3, edited by K. W. Madison, K. Bongs, L. D. Carr, A. M. Rey, and H. Zhai (World Scientific, Singapore, 2015).
41 C. Chin, Science **305**, 1128 (2004).